Journal of the Brazilian Society of Mechanical Sciences and Engineering (2021) 43:119
https://doi.org/10.1007/s40430-021-02814-y

TECHNICAL PAPER

Rotordynamic force estimation of turbulent, annular seals using OpenFOAM®

Troy Snyder[1] · **Ilmar Santos**[1]

Received: 13 October 2020 / Accepted: 10 January 2021 / Published online: 6 February 2021

Abstract

3D CFD simulations are performed to resolve the leakage rates, axial pressure drops, and dynamic force coefficients of smooth annular seals. Simulations are performed for several, simple annular seal geometries subject to water and gas flows in order to verify and validate the open-source CFD library OpenFOAM for such applications. Rotordynamic force coefficients are determined using the whirling-rotor method. Accuracy of CFD-predicted results is assessed through direct comparison with published experimental data and bulk-flow model predictions. For the three water seals analyzed, the open-source, CFD-predicted dynamic coefficients closely agree with their experimental counterparts. The k-ω family of turbulence models is shown to outperform the k-ϵ models. For the gas seals, the open-source CFD solver is shown to be unsatisfactory in predicting damping coefficients and simulations are alternatively performed with ANSYS Fluent.

Keywords Annular seal · Rotordynamics · CFD · OpenFOAM · Bulk-flow model

1 Introduction

The leakage rates and dynamic coefficients of non-contacting annular seals are most commonly predicted using models based on Reynolds equation or bulk-flow equations [1, 2]. Both the Reynolds and bulk-flow equations are simplified forms of the 3D Navier–Stokes equations which exploit the disparity of length scales associated with the thin fluid films of bearing and seal clearances. Models have many incarnations and modifications but differ primarily in their treatment of lubricant inertia, turbulence, and the approximation of the velocity profiles across the fluid film [3]. In the Reynolds equation formulation for low-R e flows, shear stresses at the rotor and stator surfaces are expressed in terms of the near-wall velocity gradients and fluid inertia is often neglected, whereas in the bulk-flow equations for high-R e flows, the wall stresses are connected to bulk film velocities through friction factors and fluid inertia plays a significant role.

Solutions of the bulk-flow equations range in complexity from space-marching methods [4–8], which assume uniformity in the circumferential flow direction with the seal, to more advanced methods based on the SIMPLE-family of numerical schemes [9–12]. The bulk-flow equations bear similar form to the 3D Navier–Stokes equations through the presence of nonlinear convective terms in the linear momentum equations and the required coupling of the continuity and linear momentum equations through pressure, barring additional simplifying assumptions.

In addition to the thin-film models, the use of 3D CFD to predict the static and dynamic performance of hydrodynamic bearings and seals has increased in frequency. Higher-fidelity CFD models are useful in examining seal operating conditions or complex geometries for which thin-film models are no longer applicable. Most notably, CFD can be used to more accurately model the inlet flow region of a seal, supplanting the use of empirical inlet loss and swirl coefficients within bulk-flow models. However, the added detail and accuracy of CFD simulations come at significantly greater computational expense than the solution of thin-film models, requiring judicious application.

In the context of 3D CFD, the dynamic coefficients of annular seals have been evaluated through three different methods: (a) perturbed equation, (b) whirling-rotor, or (c)

Editorial responsibility: Samuel da Silva.

✉ Troy Snyder
trosny@mek.dtu.dk

[1] Department of Mechanical Engineering, Technical University of Denmark, Kgs, Lyngby, Denmark

numerical shaker [13] (Instationary Perturbation Method (IPM) [14]).

In the perturbed equation method, small, harmonic perturbations of the flow variables are introduced into the Navier–Stokes and turbulence transport equations [15]. The resulting set of Taylor-series expanded equations, when solved, yields both the static flow field and rotordynamic forces/coefficients of the seal. Assuming circumferentially symmetric flow to simplify the analysis, the perturbed set of Navier–Stokes equations can be case in discrete form using finite difference [15], finite volume [16], or finite element discretization. Baskharone and Hensel [17, 18] extended earlier incarnations of the perturbation method to account for asymmetry in the circumferential flow. Like Dietzen and Nordmann [15], Arghir and Frene [19] applied a coordinate transformation to develop a perturbed set conservation equations which accommodated arbitrary whirling motions of the rotor but did not restrict the analysis to circumferentially symmetric flow. Rather, the authors [19] applied the SIMPLE (Semi-Implicit Method for Pressure Linked Equations [20, 21]) algorithm to solve both the zeroth-order, steady-state Navier–Stokes equations and their first-order counterparts.

The whirling-rotor method is limited to the analysis of rotors exercising small excursions from the seal center (Δ) which are characterized by circular whirling orbits. In the method, the 3D Navier–Stokes equations and turbulence transport equations are expressed in a rotating coordinate frame attached to the rotor and rotating at the rotor whirl speed, ω (Fig. 1). If one considers a constant whirl speed, the transformation renders the three-dimensional, transient flow field within the seal quasi-steady, circumventing the need for a more computationally expensive transient simulation. Early investigations by Tam et al. [22] and Athavale et al. [23] focused on predicting the behavior of annular seals exhibiting recirculating flow patterns due to large clearance and/or radial injection. Moore and Palazzolo [24] examined the rotordynamic forces generated by the primary and secondary flow passages in a centrifugal impeller. Other investigations have applied the whirling-rotor method to examine the performance of smooth [25]

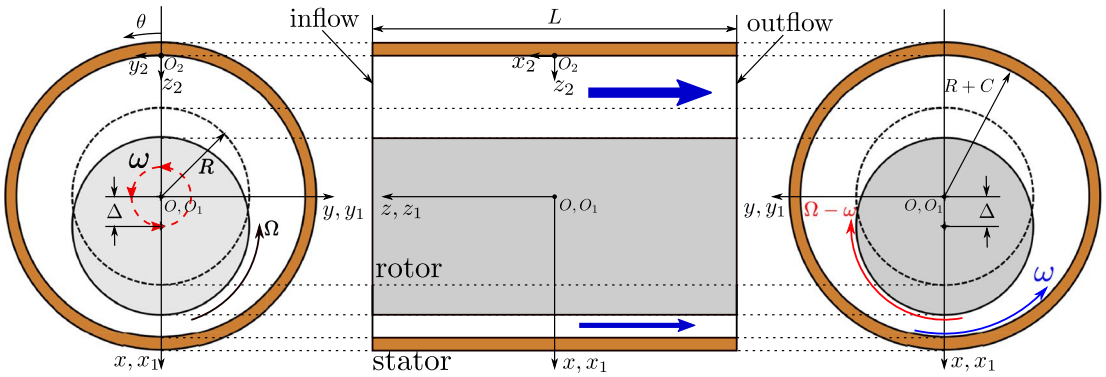

(a) Schematic of smooth, annular seal geometry

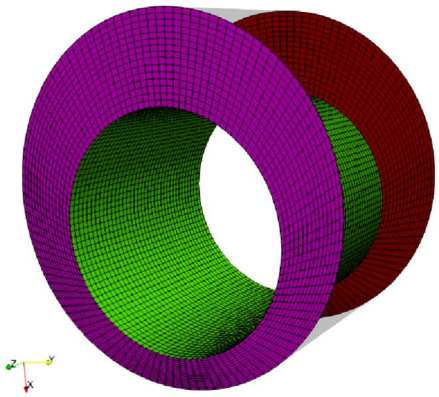

(b) Mesh e, 100x clearance.

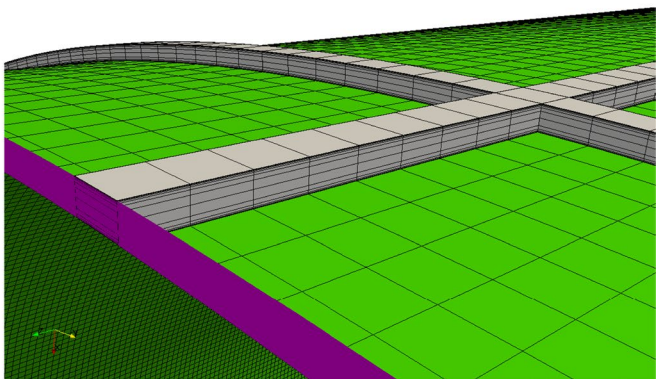

(c) Mesh g.

Fig. 1 Seal geometry and mesh. **a** Seal geometry schematic. **b** CFD mesh e (Table 7) with clearance increased 100x and $\Delta/C = 0.5$. **c** CFD mesh g with non-uniform, boundary layer mesh across clearance, and uniform mesh in axial and circumferential directions

and labyrinth [26, 27] gas seals as well as smooth [28] and grooved [29, 30] pump seals.

The numerical shaker method [13] is the analog of experimental shaker modal analysis methods. It involves the solution of the full 3D, transient Navier–Stokes equations (and additional transport equations for turbulence and/or energy) and is therefore the most computationally expensive of the three methods to determine rotordynamic forces from CFD simulation. However, the numerical shaker method is also the most flexible method which can account for complex seal geometries undergoing arbitrary (e.g., non-circular) rotor motions and nonlinear effects arising from large rotor amplitudes. In the method, the rotor or seal housing of the CFD model is given some finite, transient motion and the resulting rotor forces are curve-fit or used to form a frequency response function for subsequent identification of the rotordynamic seal force coefficients. Chochua and Soulas [31] and Nielsen et al. [14] successfully applied the numerical shaker method to predict the rotordynamic forces of hole- and honeycomb-pattern gas seals, which are difficult to model accurately using bulk-flow analysis. Voigt et al. [32] utilized the method to identify the rotordynamic forces of a smooth seal subject to droplet (wet-gas compression) and bubbly (multiphase pumping) flows.

In the present work, the whirling-rotor method is applied within a CFD framework to determine the rotordynamic coefficients, leakage rates, and axial pressure drops of smooth annular seals. Three water (incompressible) and three air (compressible gas) seals are examined and CFD-predicted results are compared with both bulk-flow model (BFM) predictions and experimental results.

Unlike most previous CFD investigations, the present work leverages the open-source CFD library OpenFOAM (OF) [33] to predict seal dynamic performance. The CFD-based modeling approach presented in this work provides improvements over previous CFD investigations in terms of increased model fidelity and the explicit demonstration of CFD result sensitivity on turbulence model type, turbulence wall function, whirling amplitude, and inlet swirl ratio. Moreover, this work specifically contributes CFD-predicted dynamic coefficients for a gas seal [58] which exhibits some anomalous behavior in stiffness coefficient and for which previous bulk-flow model predictions have varied significantly between different researchers [12, 58].

Being open-source software, OpenFOAM does not suffer from the licensing restrictions of its commercial counterparts and also benefits from increased flexibility and scalability. The licensing cost of commercial CFD software is especially prohibitive in the deployment of physics-based digital twin models (augmented with live experimental data) of rotordynamic systems with annular seals on remote, cloud-computing platforms. In such applications, having available verified and validated open-source CFD models of annular seals (and bearings) is paramount.

A detailed account of both the seal model setup and predicted performance in this work is especially useful for engineers and researchers wishing to perform similar investigations leveraging OpenFOAM. Moreover, the validation of the open-source CFD tools for the simple, well-documented seal geometries presented herein is a necessary precursor to the deployment of open-source CFD tools in the state-of-the-art analysis of multiphase seals with complex geometries. Under such conditions, the thin-film model assumptions breakdown and CFD is the only recourse for analysis.

2 Computational fluid dynamics (CFD) model

The open-source continuum mechanics library OpenFOAM [33] was used for CFD simulations of the annular seals in this work. Specifically, the solver applications `SRFSimpleFOAM` [34] and `steadyCompressibleSRFFoam` [35] were, respectively, employed to resolve incompressible and compressible seal flows. The CFD models were used to estimate axial pressure drops, leakage rates, and rotordynamic force coefficients. In addition, simulations of the gas (air) seals were performed with the commercial software ANSYS Fluent [36, 37] as the solver `steadyCompressibleSRFFoam` was found to produce unsatisfactory estimates for the seal damping coefficients.

2.1 Dynamics

A linear mechanical model of the dynamic force response of the seal was assumed for the transverse motion of the rotor about the seal center (point O in Fig. 1)

$$\begin{bmatrix} M_{xx} & 0 \\ 0 & M_{yy} \end{bmatrix} \begin{Bmatrix} \ddot{x}_0 \\ \ddot{y}_0 \end{Bmatrix} + \begin{bmatrix} D_{xx} & D_{xy} \\ D_{yx} & D_{yy} \end{bmatrix} \begin{Bmatrix} \dot{x}_0 \\ \dot{y}_0 \end{Bmatrix} + \begin{bmatrix} K_{xx} & K_{xy} \\ K_{yx} & K_{yy} \end{bmatrix} \begin{Bmatrix} x_0 \\ y_0 \end{Bmatrix} = - \begin{Bmatrix} F_{x_0} \\ F_{y_0} \end{Bmatrix} \tag{1}$$

Both the stiffness and damping matrices were assumed to be skew-symmetric: $K_{xx} = K_{yy} = K$, $K_{xy} = k$, $K_{yx} = -k$, $D_{xx} = D_{yy} = D$, $d_{xy} = d$, $d_{yx} = -d$. The direct added mass terms $M_{xx} = M_{yy} = M$ were retained for all the seals, although they proved to be negligibly small for the gas seals considered. Cross-coupled added-mass coefficients were not considered. The assumptions made for the linearized force seal force model are well-known in the literature and have been shown to be valid for small rotor motions about the seal center.

The dynamic coefficients were evaluated using CFD through the whirling-rotor method [23]. The rotor assumed a

circular whirling motion with an amplitude Δ and frequency ω about the seal center, see Fig. 1. The transient governing equations (Navier–Stokes and energy) were then cast in quasi-steady form by expressing the flow velocities in a rotating reference frame (x_1, y_1, z_1) which rotated at a constant whirl speed ω about the z-axis. The fluid within the seal was thereby rendered stationary with respect to the rotor and stator surfaces. CFD geometries were created for a fixed mesh with the whirling amplitude explicitly applied in the x_0-direction as depicted in Fig. 1. In the rotating reference frame, the surface speeds $(\Omega - \omega)R$ and $-\omega(R + C)$ were, respectively, applied to the rotor and stator.

In the rotating reference frame, the dynamic force balance embodied in Eq. 1 can be transformed [38] into simplified expressions for the radial and tangential seal forces as functions of the perturbation frequency ω

$$\begin{pmatrix} -M\omega^2 + d\omega + K \\ D\omega - k \end{pmatrix} = - \begin{pmatrix} F_r/\Delta \\ F_t/\Delta \end{pmatrix} \tag{2}$$

With Δ explicitly applied in the x-direction of the CFD model mesh (Fig. 1), F_r and F_t, respectively, coincide with F_x and F_y extracted from the model results. The dynamic coefficients were evaluated by varying the perturbation frequency ω and least-squares curve-fitting Equation 2 to the CFD-predicted seal forces. Unless otherwise noted, the frequency ratios considered for the whirling motion were $\omega/\Omega = [0, 0.25, \ldots, 1.25, 1.5]$.

2.2 Governing Equations

The steady form of Reynolds-Averaged Navier–Stokes (RANS) equations was solved for the velocity, pressure, and temperature fields within the seals. When expressed in terms of rotating coordinates, Coriolis and centrifugal acceleration terms arise in the linear momentum equation

$$\nabla \cdot \left(\rho \mathbf{v}_r \otimes \mathbf{v}_r\right) + \nabla \cdot \tau_r + \rho\left(\mathbf{a}_{\text{Coriolis}} + \mathbf{a}_{\text{Centrifugal}}\right) = -\nabla p \tag{3}$$

where $\mathbf{a}_{\text{Coriolis}} = 2\boldsymbol{\omega} \times \mathbf{v}_r$, $\mathbf{a}_{\text{Centripetal}} = \boldsymbol{\omega} \times \boldsymbol{\omega} \times \mathbf{r}$, the relative velocity is $\mathbf{v}_r = \mathbf{v} - \boldsymbol{\omega} \times \mathbf{r}$, and $\mathbf{r}$ is the position vector pointing from the rotating reference frame axis to the local cell-center. The effective shear stress τ_r includes both laminar and turbulent Reynolds stresses (eddy viscosity form) expressed in terms of the relative velocity component derivatives. In rotating coordinates, the continuity equation is obtained solely by replacing the absolute velocity $\mathbf{v}$ with the relative velocity $\mathbf{v}_r$. For the incompressible and isothermal flow simulations of water seals, a simplified form of the Navier–Stokes equations was solved using kinematic pressure as a dependent variable.

For the compressible gas seal simulations, an additional conservation equation for energy was solved and the equation of state for a perfect gas employed for the fluid (air) with $R = 287$ [J/(kg K)], $c_p = 1007$ [J/(kg K)], a molecular mass of 28.9 [g/mol], Pr $= 0.7$, and $\gamma = 1.4$. For the compressible simulations, the gas dynamic viscosity $\mu = 1.845e-7$ [N s/m^2] was held constant. The specific form of energy conservation solved within `steadyCompressibleSRFFoam` is

$$\frac{\partial}{\partial t}(\rho I) + \nabla \cdot \left(\rho \mathbf{v}_r I\right) - \nabla^2(\alpha I) = -\tau_r : \nabla \mathbf{v}_r \tag{4}$$

where $\alpha = k/c_p$ is the thermal diffusivity and $I = h + 0.5\left(|\mathbf{v}_r|^2 - |\boldsymbol{\omega} \times \mathbf{r}|^2\right)$ is the rotational stagnation enthalpy or rothalpy, $\nabla^2(\alpha I)$ is diffusive heat transport (conduction), and $\tau_r : \nabla \mathbf{v}_r = \left(\tau_r\right)_{ij}\left(\nabla \mathbf{v}_r\right)_{ij}$ is the effective viscous dissipation.

In ANSYS Fluent [37], the RANS equations expressed and solved in a rotating reference frame bear a similar form to those within the `SRFSimpleFoam` and `steadyCompressibleSRFFoam` solvers for incompressible and compressible flows, respectively.

2.3 Turbulence modeling

For the first water seal considered in this work, both $k - \omega$ and $k - \epsilon$ families of turbulence models were employed and the resulting dynamic coefficients and axial pressure drops compared. Given the presence of significant pressure gradients (although favorable), rotation, and mean streamline curvature in annular seal flows, the $k - \omega$ family of turbulence models was thought likely to provide more accurate results compared with the $k - \epsilon$ models, the latter of which are known to have difficulties modeling such flow behavior [39]. It will be shown subsequently that the $k - \omega$ model family does indeed outperform the $k - \epsilon$ model family in the prediction of axial pressure drop and dynamic coefficients of a typical annular pump seal. Turbulence in the remaining seals was modeled using the $k - \omega$ SST model only.

A priori estimates of shear stresses were used to determine the wall-adjacent mesh cell heights required to obtain $y^+ \approx 1.0$, where $y^+ = u^* y/\nu$ is a function of the friction velocity $u^* = \sqrt{\tau_w/\rho}$. The wall shear stress, $\tau_w = 0.5 f \rho \bar{v}_z^2$, was estimated with the friction factor approximated by the Swamee-Jain [40] equation and considering the root-mean-squared (RMS) value of the axial and circumferential Reynolds numbers of the seal with zero wall roughness and the average axial velocity $\bar{v}_z$. The axial and circumferential Reynolds numbers were evaluated using the hydraulic diameter and the radial clearance of the seal, respectively.

For the OpenFOAM RANS simulations, the turbulent wall viscosity was evaluated using Spalding's universal function [41]. For the compressible ANSYS Fluent simulations, the $k - \omega$ SST turbulence model was employed with

enhanced wall function treatment [37] which blends laminar and turbulent laws-of-the-wall to provide continuous and asymptotically correct values for all y^+. Generally, seal leakage rates and radial forces predicted with ANSYS Fluent were found to be slightly less sensitive to near-wall mesh cell height size compared with those obtained with OpenFOAM, likely attributable to differences in wall function formulations. At the inflow boundary, the turbulent kinetic energy and dissipation rate were estimated using a turbulence intensity of 5% and radial clearance, C, as length scale. The turbulence parameters at the outflow were extrapolated from the domain interior.

2.4 Boundary conditions

For the incompressible flow simulations, the seal inflow velocities were first prescribed using the `swirlInletVelocity` boundary condition for which axial velocity was prescribed using the experimental value (estimated from leakage rate) along with swirl velocity. A zero gradient condition was prescribed for the pressure. After a converged solution was obtained with the prescribed velocity boundary condition, the inflow pressure was changed to a fixed value (extrapolated from the interior) and the model was re-run until convergence. This two-step solution process ensured the leakage rate and its circumferential variation was consistent with experimental findings. The outflow static pressure was held constant at atmospheric pressure (zero gauge pressure) and the velocities were extrapolated from the interior of the domain.

For the compressible flow simulations of the gas seals, a total temperature of 300 [K] was imposed at the inflow boundary along with the total pressure. At the inflow, static pressures and temperatures were evaluated using isentropic flow relations, $p = p_0\left(1 + 0.5(\gamma - 1)\,\mathrm{M\,a}^2\right)^{-\gamma/(\gamma-1)}$ and $T = T_0\left(1 + (\gamma - 1)\,\mathrm{M\,a}^2\right)^{-1}$, respectively. At the outflow boundary, the static pressure was prescribed and the static temperature was extrapolated from the interior. The pressures applied at the inflow and outflow boundaries were taken directly from experiment which typically presented leakage rates and seal force coefficients in terms of inflow–outflow pressure ratio, P_i/P_e. The experimental pressures were directly applied at the inflow and outflow boundaries of the CFD model without consideration of inflow loss or outflow recovery effects. In contrast to the water seals, neglecting the inlet losses of the gas seals did not introduce significant error into the predicted leakage rates and dynamic coefficients evidenced in Figs. 6 and 9.

At the rotor and stator walls, the relative velocities were prescribed based on the rotor rotational and preccessional speeds, and the pressures were extrapolated from the domain interior (zero gradient). The wall temperatures were held constant at 300 [K].

2.5 Solution details

The incompressible and compressible forms of the governing equations were cast in discrete form using the finite-volume method [42] and iteratively solved with the original SIMPLE algorithm [21] or its extended form for compressible flows [43]. Cell-centered gradients were constructed using a least-squares approach, as this was generally found to provide a modest improvement in accuracy compared with a Green-Gauss, cell-based approach. In Fluent simulations, convective fluxes were discretized using second-order upwinding and similar accuracy was achieved in OpenFOAM by setting the discretization scheme for `div(phi,U)` to `Gauss linearUpwind grad(U)`. For compressible simulations, advective transport terms within the energy equation were discretized using first-order upwinding to ensure boundedness and promote solution stability.

A threshold value of $1e-5$ was applied to the normalized residuals of continuity and linear momentum equations to signify convergence. A stricter convergence criteria were applied to the energy equation in the compressible flow simulations, with a residual threshold of value of $1e-6$. A threshold value of $1e-4$ was considered for the residuals of the turbulence transport equations. The convergence criteria were successfully achieved for all the seals except gas seal [44] at larger pressure ratios, for which the continuity residuals would not fall below $3e-4$. However, for this seal, the leakage rate converged to within three significant digits. For all the remaining seals, residual convergence corresponded to leakage rate convergence to within four significant digits.

In OpenFOAM, pressure and velocity under-relaxation factors of 0.3 and 0.7 were, respectively, employed. For the compressible flow simulations, the relaxation factors for velocity and density were set to 0.5 and 0.1 for rothalpy. Turbulence under-relaxation factors of 0.5 were employed for k and ϵ or ω. In ANSYS Fluent, the default values of the under-relaxation factors [36] proved sufficient for compressible flow simulations.

A flowchart of the overall process by which the dynamic coefficients are extracted from the OpenFOAM CFD simulations is shown in Fig. 2.

3 Bulk-flow model (BFM)

To complement comparisons between experimental measurements and CFD predictions of seal leakage rates and dynamic coefficients, model predictions were also made by solving the bulk-flow conservation equations of mass, linear momentum [45], and energy

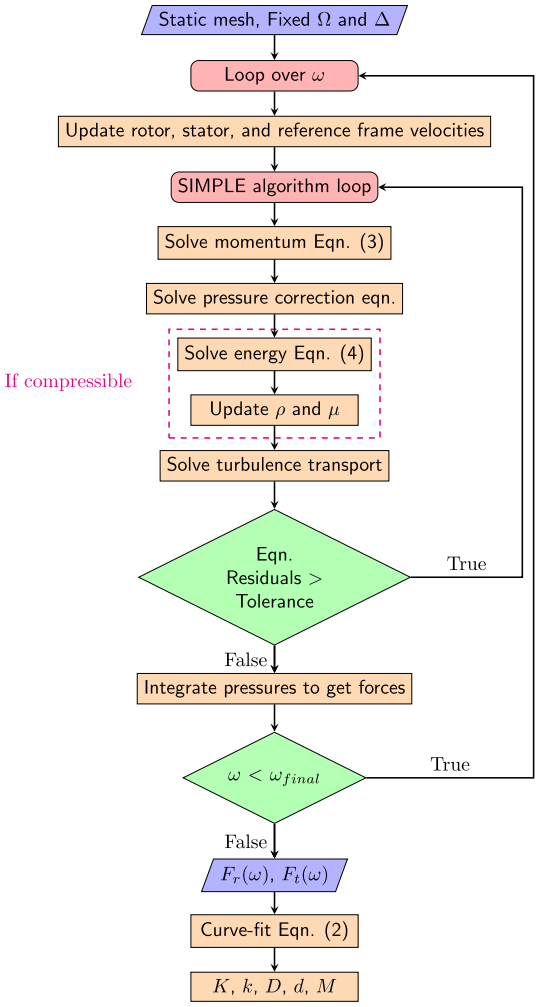

Fig. 2 Flowchart of dynamic coefficient calculation using OpenFOAM rotating reference frame solver applications

$$\frac{\partial(\rho h)}{\partial t}+\frac{\partial\left(\rho h\overline{u}\right)}{\partial x}+\frac{\partial\left(\rho h\overline{v}\right)}{\partial y}=0 \tag{5}$$

$$\frac{\partial\left(\rho h\overline{u}\right)}{\partial t}+\frac{\partial\left(\rho h\overline{u}^{2}\right)}{\partial x}+\frac{\partial\left(\rho h\overline{uv}\right)}{\partial y}=-\frac{\partial p}{\partial x}h+\tau_{xz,r}-\tau_{xz,s} \tag{6}$$

$$\frac{\partial\left(\rho h\overline{v}\right)}{\partial t}+\frac{\partial\left(\rho h\overline{vu}\right)}{\partial x}+\frac{\partial\left(\rho h\overline{v}^{2}\right)}{\partial y}=-\frac{\partial p}{\partial y}h+\tau_{yz,r}-\tau_{yz,s} \tag{7}$$

$$c_p\left(\frac{\partial\left(\rho h\overline{T}\right)}{\partial t}+\frac{\partial\left(\rho h\overline{u}\overline{T}\right)}{\partial x}+\frac{\partial\left(\rho h\overline{v}\overline{T}\right)}{\partial y}\right)=-\left(q_z\right)_{h_s}^{h_r} - \left(\tau_{zx}\overline{u}+\tau_{zy}\overline{v}\right)_{h_s}^{h_r}+\alpha_v\overline{T}h\left(\frac{\partial p}{\partial t}+\overline{u}\frac{\partial p}{\partial x}+\overline{v}\frac{\partial p}{\partial y}\right) \tag{8}$$

The bulk-flow equations govern the flow through the seal under the simplifying assumption that the seal clearance is an order-of-magnitude smaller than its length and diameter. The equations in their form above apply to an unwrapped seal geometry with local coordinate system (x_2, y_2, z_2) (Fig. 1) for which the coordinates, respectively, correspond to the axial, circumferential, and normal (across-the-film) directions. The inertia terms in the bulk-flow equations above were derived assuming uniform velocity profiles across the clearance film, a reasonable approximation for fully developed turbulent flow.

The presence of inertia terms in the bulk-flow momentum equations precludes expressing wall shear stresses solely through film pressure gradients. Shear stresses at the rotor and stator walls are related to the bulk-flow velocities through shear coefficients [3, 46] or, as in the present work, through fanning friction factors [2, 6, 45]

$$\tau_{xz,r}-\tau_{xz,s}=-0.5\rho\left(U_sf_s+U_rf_r\right)\overline{u} \tag{9}$$

$$\tau_{yz,r}-\tau_{yz,s}=-0.5\rho\left(U_sf_s\right)\overline{v}-0.5\rho\left(\overline{v}-R\Omega\right)U_rf_r \tag{10}$$

where U_r and U_s are the rotor and stator surface velocity magnitudes relative to the bulk flow.

Various friction factor formulas have been applied by previous investigators in the analysis of annular seals, the most common of which being pipe friction models based on a Blasius-type expression [2] or approximate correlations fit to the Moody chart [47]. Moody-based friction formulas can advantageously account for surface roughness which has been shown to significantly affect the stiffness and damping coefficients of intentionally roughened annular seals [48]. However, in the present work, the rotor and stator surfaces were considered hydraulically smooth in applying the Haaland approximation for the Moody friction factor.

In the bulk-flow approach applied in this work, the dynamic coefficients were solved using perturbation theory where the flow variables were decomposed as $\phi=\phi_0+\varepsilon\phi_i\exp\left[i\omega t\right]$ where $\varepsilon << 1$, and where ϕ represents an arbitrary perturbed variable. The introduction of this decomposition into the transient bulk-flow equations resulted in zeroth- and first-order (linearized) differential equations for the flow variables. The zeroth-order system of equations was solved for the leakage rate and static forces and the first-order equations, once solved for the dynamic pressures, yielded the seal dynamic coefficients (stiffness,

damping, added-mass). For incompressible flows, the perturbed variables included the film thickness, velocities, and pressure. For compressible flows, the density and temperature were additionally considered as perturbation variables. One is referred to the extensive literature for more details on the development of perturbed bulk-flow equations for incompressible [6, 49] and compressible [8, 12] seal flows.

4 Modeling errors

The CFD model of water seal 1 tested by Kanki and Kawakami [50] was used to assess errors related to mesh size, RANS turbulence model, and whirling amplitude. Computational meshes were generated using OpenFOAM's `blockMesh` utility.

4.1 Mesh convergence

The reaction forces and axial pressure drop estimated using OpenFOAM are summarized in Fig. 3 for varying number of total mesh cells. The figure plots include three lines corresponding to 10, 15, or 20 mesh cells distributed across the seal clearance. The plots also include labels ($a - m$) with the mesh parameters defined in Table 7 of the Appendix.

A uniform mesh e with an exaggerated seal clearance is provided in Fig. 3 to visualize the eccentric rotor position applied in the CFD model. In Fig. 3, the non-uniform, boundary layer mesh g is shown with the physical seal dimensions. Meshes a, e, and j were uniform in all directions while the remaining meshes were generated with non-uniform cell distributions across the seal clearance to reduce y^+ near the rotor and stator surfaces. Wall-adjacent mesh cell heights, $y = y^+\nu/u^*$, were estimated using the procedure described in Section 2.3. The number of mesh cells in the axial and circumferential directions was then determined using y, the seal dimensions, and a constraint that the cell aspect ratios remained less than 1000. All meshes generated with preliminary $y^+ = 1$ resulted in post-simulation calculations of $y^+ \leq 1$ (Table 7) as desired. This meshing procedure was also applied to generate the meshes for the remaining seals in this work, resulting in different mesh sizes due to differences in seal dimensions and Reynolds numbers.

In Fig. 3, convergence of the reaction forces and pressure drop is visible for meshes with 15 and 20 cells distributed across the seal clearance. Notably, convergence in the axial pressure drop is obtained at reduced mesh sizes compared with the reaction forces. Utilizing results for meshes c, g, and m, the Grid Convergence Index (GCI) [51] error estimates associated with mesh g for the radial forces and the axial pressure drop were found to be acceptably small: $\varepsilon_{F_x} = 4.8\%$, $\varepsilon_{F_y} = 5.6\%$, and $\varepsilon_{\Delta P} = 5.7\%$. Additionally, the dynamic coefficients evaluated on mesh g using the $k - \omega$ SST turbulence model are listed in Table 1. The errors relative to the averaged experimental results were found to be: $\varepsilon_K = -0.69\%, \varepsilon_k = -5.56\%, \varepsilon_D = -3.40\%, \varepsilon_d = +10.8\%$ and $\varepsilon_M = +44.9\%$. The dynamic coefficients on mesh g were deemed to be of sufficient accuracy while maintaining tractable mesh size for the number of simulations required. The added mass and, to a lesser degree, the cross-coupled damping coefficients were not as well-predicted, but these coefficients are notoriously difficult to predict accurately and may be influenced by inflow and outflow geometric features

Table 1 Variation in CFD-predicted dynamic coefficients with turbulence model for water seal 1 [50]

	K_{xx} K_{yy}	K_{xy} K_{yx}	D_{xx} D_{yy}	D_{xy} D_{yx}	M_{xx} M_{yy}
	[MN/m]		[kN s/m]		[kg]
Exp. [50]	3.30	11.3	147	52.9	229
	3.89	−10.3	147	−57.7	214
$k - \omega$	3.38	±9.80	104	±68.6	343
$k - \omega$ SST	**3.57**	**±10.2**	**142**	**±61.3**	**321**
$k - \epsilon$	5.78	±23.4	257	±61.6	312
$k - \epsilon$ RNG	6.30	±21.3	242	±61.8	312

Bold values indicate the most accurate/best results

Nominal mesh, $SR = 0.3$, RANS, two-equation eddy viscosity turbulence models

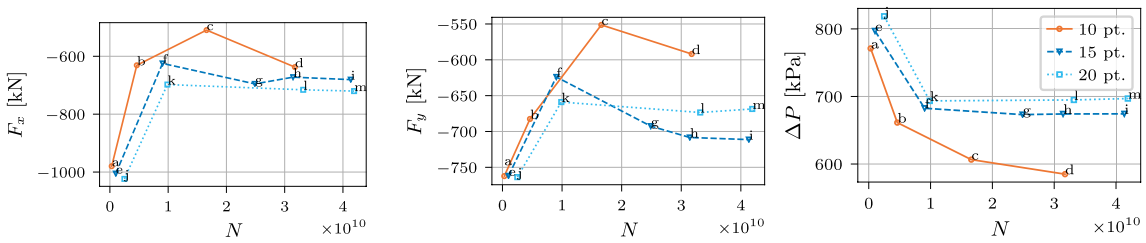

(a) F_x [kN] **(b)** F_y [kN] **(c)** ΔP [kPa]

Fig. 3 Convergence of radial forces and axial pressure drop with increasing overall number of mesh cells N for seal 1 [50]. $\Delta/C = 0.2$, $\omega/\Omega = 0.5$, $k - \omega$ SST

not included in the model. Based on these results, 15 cells were used across the clearance in generating the meshes for the additional seals considered.

In the present work using OpenFOAM, smaller values of y^+ and substantially larger overall mesh sizes compared with previous investigations employing commercial CFD software [25, 28, 32] were required to obtain accurate results. Additionally, large cell growth ratios (Table 7) were required in the present work to move the near-wall cell center outside the buffer layer $5 < y^+ < 30$. This appears to be a result of differences between Spalding's original universal wall function [41] used in OpenFOAM and the enhanced law-of-the-wall and blending employed commercial software such as ANSYS Fluent (Sec. 4.12.4 [37]), the latter of which both reduce y^+ sensitivity.

4.2 Effect of RANS turbulence model

RANS turbulence models from both the $k-\omega$ and the $k-\epsilon$ families were applied in the simulation of the water seal 1 [50]. The predicted dynamic coefficients using the various turbulence models are summarized in Table 1. Also, included are the experimental values [50] for which the mutually perpendicular directions exhibited nearly equal coefficients for the concentric seal tested. Based on the results in Table 1, the dynamic coefficients predicted with OpenFOAM using the $k-\omega$ SST model [52] are in closest agreement with the experimental values, followed by the standard $k-\omega$ model. For the $k-\omega$ SST model results, the errors in all the stiffness and damping coefficients remain below 11%, with the errors in the direct stiffness and damping coefficients remaining below 4%. Note that the realizable $k-\epsilon$ model was also tested, but convergence could not be obtained for some of the meshes and perturbation frequencies considered. For those cases that did converge, the results typically fell between those of the standard and RNG $k-\epsilon$ models.

In Table 1, the direct and cross-coupled stiffness coefficients, as well as the direct damping coefficients, predicted using the $k-\epsilon$ family of turbulence models exceed their experimental values by approximately 100%. The cross-coupled damping coefficients show agreement with the experimental values and those predicted using the $k-\omega$ family of models. The added mass coefficients predicted using the $k-\epsilon$ and $k-\omega$ turbulence model families also show relatively close agreement with each other but exceed the experimental values by approximately 50%. Agreement between the cross-coupled damping and added-mass coefficients predicted using the $k-\epsilon$ and $k-\omega$ turbulence model families suggests that these coefficients may be more heavily influenced than the other coefficients by the seal inflow and outflow features not included in the model.

Similar to the dynamic coefficients, the CFD-predicted axial pressure drop (frictional only) along the seal differs substantially between turbulence model families but is similarly predicted within a given model family. Corresponding to Table 1, ΔP predicted by the $k-\omega$ and $k-\omega$ SST models are 687 and 662 [kPa], respectively. ΔP predicted by the standard and RNG $k-\epsilon$ models are 1.56 and 1.46 [MPa], respectively. One can directly correlate these pressure drops to the variations in the direct stiffness coefficients predicted by the various turbulence models. The total ΔP obtained from experiment, which includes both the frictional pressure drop along the seal and non-recoverable pressure drop at the seal inflow, is 980 [kPa], which makes the $k-\epsilon$ family results non-physical.

Differences in the predicted dynamic coefficients and pressure drops between the turbulence models also correlate to the variations in the velocity and eddy viscosity profiles within the seal depicted in Fig. 4. The larger values of direct stiffness and ΔP predicted by the $k-\epsilon$ models compared with the $k-\omega$ models correspond with reduced centerline axial velocities in Fig. 4 and larger eddy viscosity values in Fig. 4. This is physically intuitive as the larger values of eddy viscosity would retard the axial flow leading to a rise in the static pressure drop and direct stiffness. Additionally, the cross-coupled stiffness is predominantly controlled by the tangential flow in the seal which is driven by the rotor speed and inflow preswirl. In Fig. 4, moving away from the rotor surface, the velocity decays more rapidly for the $k-\omega$ models compared with the $k-\epsilon$ models leading to lower overall strength of the tangential/circumferential flow and reduced cross-coupled stiffness coefficients.

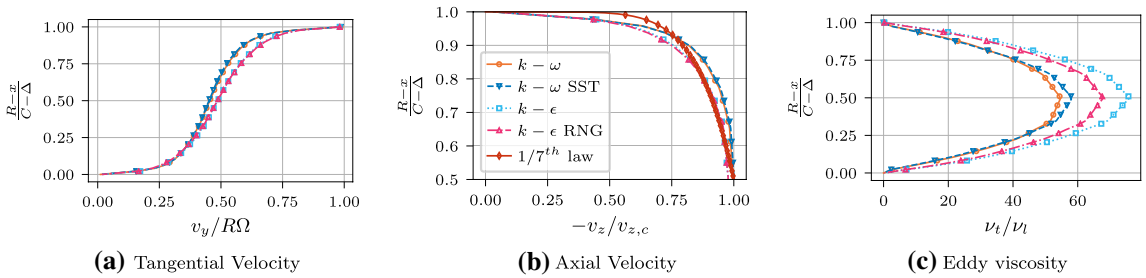

(a) Tangential Velocity **(b)** Axial Velocity **(c)** Eddy viscosity

Fig. 4 Variation in dimensionless velocity and eddy viscosity profiles RANS turbulence model. Line along x-dir. at midspan of seal 1 [50]. $R-x/(C-\Delta)=1.0$ is the non-dimensional film height corresponding to the rotor surface. $\Delta/C=0.2$, $\omega/\Omega=0.5$, mesh g (Table 7)

4.3 Whirling amplitude

In the whirling-rotor CFD method, the computational mesh was generated with a finite whirling amplitude Δ explicitly applied to the rotor surface. Δ could not be made overly small as the CFD-predicted forces became saturated with numerical error. Moreover, Δ could not be made too large as the linear description of the seal forces would cease to be valid. For the seals evaluated in this work, $\Delta = 0.2C$ was found to provide a reasonable balance between these two limits. If the whirling For $\Delta/C < 0.1$, the CFD-predicted dynamic coefficients began to deviate from their experimental values, most notably the direct and cross-coupled damping coefficients. For $\Delta/C > 0.3$, retaining a linearized model for the seal force response resulted in erroneous over- and under-prediction of the damping and cross-coupled stiffness coefficients, respectively. Notably, however, the direct stiffness and added-mass coefficients were found to be less sensitive to the whirling amplitude and could be accurately predicted up to $\Delta/C = 0.5$.

5 Results and discussion: water seals

CFD simulations of the water seals were performed with the application solver `SRFSimpleFoam` in OpenFOAM ver.5.0. The geometric and operating parameters of the water seals considered are summarized in Table 2.

5.1 Kanki and Kawakami [50] water seal 1

The first seal for which OpenFOAM CFD was exercised for the evaluation of seal dynamic coefficients was the smooth, water pump "seal 1" tested by Kanki and Kawakami [50]. The seal ($R = 100$ [mm]) was modeled using water with constant properties ($\mu = 8.780e-4$ [N s/m^2], $\rho = 996.9$ [kg/m^3]) and considering a leakage $Q = 4634$ [cm^3/s], an average axial velocity $\overline{v}_z = 14.714$ [m/s], and rotational speed $\Omega = 2000$ [rpm].

The inlet swirl ratio for the CFD model was fixed at $SR = 0.3$, a value obtained by simultaneously optimizing SR and ξ_i for a bulk-flow model [45]. Optimal values $SR = 0.303$ and $\xi_i = 0.798$ were found to minimize the sum-of-squares error between the bulk-flow predicted and the experimentally measured axial pressure drop (total) and dynamic coefficients. This optimal set of parameter values was obtained using an incompressible BFM with a prescribed (fixed) inlet axial velocity rather than a prescribed total pressure drop across the seal, the latter of which being more common in the application of BFMs.

Table 2 Summary of water seal geometric and operating parameters

	C/R	L/R	Re_a	Re_Ω
Seal 1 [50]	0.005	2.0	16, 707	11, 890
Seal 2 [50]	0.005	0.4	36, 253	13, 216
Refs. [15, 53]	0.0085	1.0	9, 368	1, 401 … 4, 201

5.1.1 Effect of inlet swirl

The effect of inlet swirl ratio (SR) on the CFD-predicted dynamic coefficients is summarized in Table 3. The direct stiffness decreases monotonically with increasing SR. The cross-coupled stiffness and cross-coupled damping coefficients increase monotonically with increasing SR. The direct damping and direct added mass coefficients remain nearly constant with changing SR. These observable trends are consistent with incompressible BFM predictions, verifying the two-stage process used for the inflow boundary condition on the CFD model.

5.1.2 Summary of results

The CFD- and BFM-predicted dynamic coefficients from the present analysis are summarized in Table 4 along with the experimental values and BFM predictions published in the literature [11, 54, 55]. The CFD-predicted stiffness and damping coefficients closely agree with their experimental counterparts. However, the direct added-mass coefficients are over-predicted by approximately 40% similar to results obtained with the BFMs.

In Table 4, the BFM results were obtained using the experimental, axial pressure drop (total) of 980 [kPa] and leakage rate serving as model input and output, respectively. For all the BFMs, to varying degree, the leakage rates were predicted in excess of the experimental values. Leakage rates of 5.17, 4.94, 4.83 [kg/s] were, respectively, predicted by the present BFM, San Andres [11], and Simon and Frene [55] models. The experimentally measured leakage rate is 4.61 [kg/s]. SR and ξ_i for the present BFM were manually tuned to best-match the experimental stiffness and damping

Table 3 Variation in CFD-predicted dynamic coefficients with inlet swirl ratio, SR, for water seal 1 [50]

	K_{xx}	K_{xy}	D_{xx}	D_{xy}	M_{xx}
	K_{yy}	K_{yx}	D_{yy}	D_{yx}	M_{yy}
	[MN/m]		[kN s/m]		[kg]
Exp. [50]	3.30	11.3	147	52.9	229
	3.89	−10.3	147	−57.7	214
$SR = 0.0$	4.07	±4.51	149	±54.7	325
$SR = 0.1$	3.93	±6.47	149	±55.7	316
$SR = 0.2$	3.71	±8.46	146	±59.8	324
$SR = 0.3$	3.57	±10.2	142	±61.3	321
$SR = 0.4$	3.24	±12.6	144	±64.9	322
$SR = 0.5$	2.97	±14.8	143	±67.5	321

Table 4 Summary of CFD- and BFM-predicted dynamic coefficient for water seal 1 [50]. Present results obtained with $SR = 0.3$ and $\xi_i = 0.2$ (BFM). $SR = 0.2$ and $\xi_i = 0.3$ applied in Refs. [11, 55]

	K_{xx} K_{yy}	K_{xy} K_{yx}	D_{xx} D_{yy}	D_{xy} D_{yx}	M_{xx} M_{yy}
	[MN/m]		[kN s/m]		[kg]
Exp. [50]	3.30	11.3	147	52.9	229
	3.89	−10.3	147	−57.7	214
Present CFD	**3.57**	**±10.2**	**142**	**±61.3**	**321**
Present BFM	3.83	±11.6	163	±71.7	323
Ref. [54]	7.80	±15.0	160	±1.0	-
Ref. [11]	3.65	±12.4	165	±58.4	305
Ref. [55]	3.77	±11.1	170	±57.6	309

Bold values indicate the most accurate/best results

coefficients, differing from the optimized values used in Refs. [11, 55]. Most notably, applying $SR = 0.2$ [11, 55] to the present BFM or CFD model resulted in substantial under-prediction the cross-coupled stiffness.

5.2 Kanki and Kawakami [50] water seal 2 (short)

The next water seal considered was the short, smooth, water pump "seal 2" tested by Kanki and Kawakami [50]. The reduced length of the seal substantially increased leakage rate and the axial Reynolds number given the same axial pressure drop of 980 [kPa] applied to the long water "seal 1" [50]. The seal ($R = 100$ [mm]) was modeled using water with constant properties ($\mu = 7.888e-4$ [N s/m^2], $\rho = 995.5$ [kg/m^3]) and considering a leakage $Q = 9047$ [cm^3/s], an average axial velocity $\bar{v}_z = 28.762$ [m/s], and rotational speed $\Omega = 2000$ [rpm].

The present CFD- and BFM-predicted dynamic coefficients for the seal are summarized in Table 5. The CFD-predicted stiffness coefficients agree with the experimental results, present BFM, and the BFM results of [11, 56]. The CFD model, like the BFMs, under-predicts the direct and cross-coupled damping coefficients of the seal. San Andres [11] attributed the discrepancy in the damping coefficients to an exit pressure which deviates from the assumed ambient pressure or to a discharge-inertia effect. Either the cause, the present CFD analysis supports an increased role in the seal end-effects in controlling the damping behavior of the seal.

The CFD-predicted static, axial pressure drop $\Delta P = 416$ [kPa] of the seal was substantially reduced from the value predicted $\Delta P = 662$ [kPa] for the longer seal examined in the previous section. The frictional pressure drop of the shorter seal constitutes a smaller percentage of the total pressure drop with increased viscous dissipation at both the seal inlet making up the remaining account of total, axial pressure drop.

Overall, the CFD- and BFM-predicted dynamic coefficients of the short seal were found to be less accurate than

Table 5 Summary of CFD- and BFM-predicted dynamic coefficients for water seal 2 [50]

	K_{xx} K_{yy}	K_{xy} K_{yx}	D_{xx} D_{yy}	D_{xy} D_{yx}	M_{xx} M_{yy}
	[MN/m]		[kN s/m]		[kg]
Exp. [50]	3.96	0.664	24.82	12.3	–
	4.01	−0.337	24.46	−10.88	–
Present CFD	**3.48**	**±0.650**	**10.8**	**±0.385**	**2.0**
Present BFM	3.76	±0.628	11.78	±0.674	2.98
Ref. [54]	3.80	±0.550	5.60	±0.03	–
Ref. [56]	3.82	±0.440	11.60	±0.56	3.58
Ref. [11]	4.01	±0.379	11.56	±0.60	3.82

Bold values indicate the most accurate/best results

Present results obtained with $SR = 0.3$ and $\xi_i = 0.3$ (BFM). $SR = 0.2$ and $\xi_i = 0.3$ applied in Refs. [11, 54, 56]

the long seal examined in the previous section. The authors believe that this is a result of the increased role of end effects for short versus long annular seal. The authors believe that the addition of inflow and outflow features of the seal geometry within the CFD model would likely improve the results, but such geometric details are not provided in Ref. [50] precluding direct investigation for this seal.

5.3 Dietzen and Nordmann [15] water seal

OpenFOAM CFD was also used to predict the dynamic coefficients of the smooth annular seal detailed in [15] considering the experimental data taken from [53]. The seal ($R = 23.5$ [mm]) was modeled using water with constant properties ($\mu = 7.0e-4$ [N s/m^2], $\rho = 996.0$ [kg/m^3]) and considering an average axial velocity $\bar{v}_z = 16.46$ [m/s] and a range of rotational speeds $\Omega = 2000-6000$ [rpm]. For both the present CFD and bulk-flow models, the inlet swirl was fixed to half the rotation speed, $SR = 0.5$, which was found to produce the most accurate results.

The dynamic coefficients predicted by the present CFD model and BFM are summarized in Fig. 5. The CFD-predicted direct stiffness and direct damping coefficients compare well with their experimental values, with direct stiffness under-predicted by approximately 18%. The present CFD model and BFM predicts cross-coupled stiffness and damping coefficients which agree both in trend and magnitude with the perturbed Navier–Stokes model of Dietzen and Nordmann [15]. The CFD model of Wagner et al. [38] deviates from the present CFD model predictions, most notably at slower rotational speeds, as the authors did not prescribe any pre-rotation to the fluid entering the seal. Additionally, the authors [15, 38] employed the standard $k-\epsilon$ turbulence model, standard wall functions, and uniform meshes spanning the seal clearance (5 and 12 cells in [15]

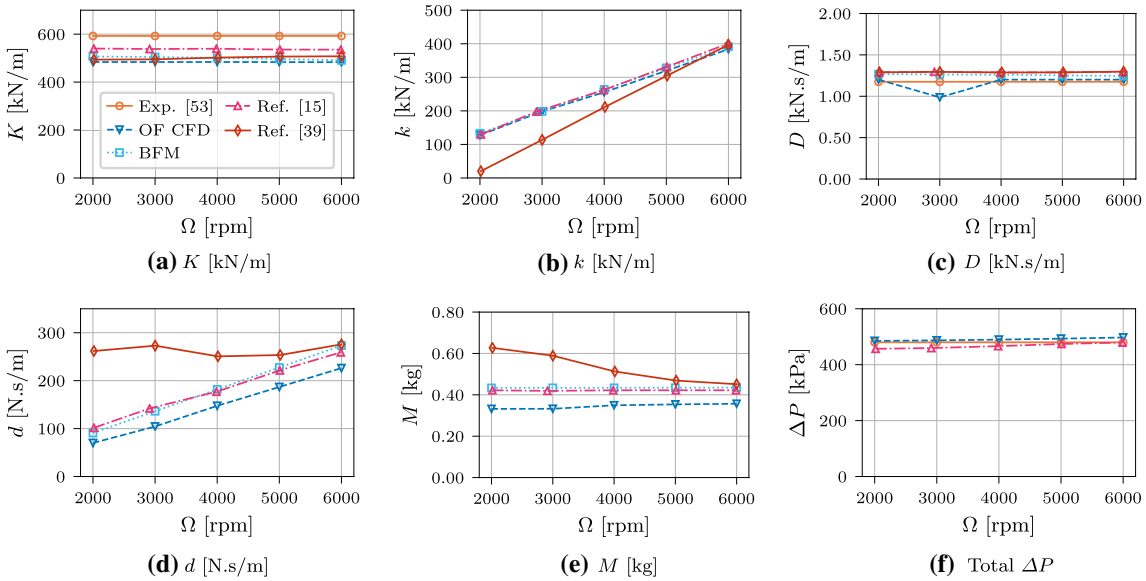

Fig. 5 Summary of CFD- and BFM-predicted dynamic coefficients for water seal [15, 53] versus rotational speed. Present CFD- and BFM-predicted results obtained using $SR = 0.5$ and $\xi_i = 0.5$. Comparison with perturbed [15] and whirling-rotor [38] CFD models

and [38], respectively), which were found to produce significant uncertainty in the results obtained in the present CFD analysis. The CFD-predicted static (frictional) pressure drop along the seal was $\Delta P = 283$ [kPa]. Considering typical seal inlet loss $\xi_i = 0.5$ and outlet recovery $\xi_o = 1.0$ coefficient values, the CFD-predicted total pressure drop along the seal would be $\Delta P = 485$ [kPa], consistent with the experimental value of $\Delta P = 480$ [kPa].

For the short seal $L/R = 0.4$ [50] examined in the previous section, the CFD-predicted direct damping coefficients were much less accurate than for the present seal $L/R = 1.0$ [15]. This is due directly to the increased length of the present seal [15] and through its lower axial Reynolds number (9, 368 [15] versus 36, 253 [50]) which reduce the seal's sensitivity to inflow and outflow effects.

6 Results and discussion: gas seals

In addition to water seals (e.g., pumps), the whirling-rotor CFD method was also used to predict the dynamic coefficients and leakage rates for three different gas (air) seals (e.g., compressors). The OpenFOAM solver `steadyCompressibleSRFFoam` was initially employed, but the damping coefficients were found to be unsatisfactorily predicted and OpenFOAM was supplanted by ANSYS Fluent. Simulations using an alternative compressible flow solver `rhoSimpleFoam` [34], which has moving reference frame capability, could not be successfully obtained due to difficulties in assigning a rotating cell zone to the small seal clearance. For the first gas seal considered [57], dynamic coefficients and leakage rates predicted with both OpenFOAM and ANSYS Fluent are compared. For the remaining gas seals [44, 58], only results predicted using ANSYS Fluent are presented. The geometric and nominal operating parameters of the gas (air) seals considered are summarized in Table 6.

6.1 Dunn [57] gas (air) seal

For the first gas seal considered [57] ($R = 76.2$ [mm], $C = 0.229$ [mm]), the seal inlet pressure was fixed at 7.86 [bar] and the exit pressure was varied as [4.339, 3.836, 3.2, 2.657] [bar]. A rotor speed of 5030 [rpm] and $SR = 0$ was applied to the model along with perturbation frequency ratios $\omega/\Omega = [0, 0.1, 0.2, 0.3, 0.4, 0.5, 0.6]$ to facilitate comparison with the results obtained by Ha and Choe [25].

In Fig. 6, the leakage rates of the gas seal [57] are plotted for varying inlet-to-outlet pressure ratio. The leakage rates predicted using both OpenFOAM and ANSYS Fluent CFD closely agree with the BFM- and CFD-based results obtained by Ha and Choe [25] and with leakage rates

Table 6 Summary of gas seal geometric and operating parameters

	C/R	L/R	Re_a	P_i/P_e
Dunn [57]	0.003	0.67	1.81e6	2.21
Ransom et al. [58]	0.003	0.64	4.84e5	2.27
Elrod et al. [44] 'C01'	0.009	0.67	3.49e6	2.23

Re_a evaluated using experimental leakage rate at P_i/P_e listed and viscosity $\mu = 1.845e-7$ [N s/m^2]

exceeding their experimental values by approximately 20% at all pressure ratios.

In Fig. 6, the direct stiffness coefficients predicted in the present analysis using ANSYS Fluent closely agree with the experimental values. Notably, all of the CFD-based results more closely match the experimental direct stiffness coefficients, which are over-predicted by the BFMs for the entire range of pressure ratios. All of the model-predicted direct stiffness coefficients exhibit the same trend as their corresponding experimental values.

In Fig. 6, the CFD and BFM results for cross-coupled stiffness exhibit close agreement with each other but under-predict the experimental values approximately by a factor of 2. The model-predicted cross-coupled stiffness values exhibit a slight increase with increasing pressure which is not clearly mirrored in the experimental results. This discrepancy is likely a result of not applying adequate inflow pre-rotation to the model, which was not directly provided in the experimental description [57]. However, the absence of fluid pre-rotation in the model fails to explain the over-predicted leakage rates in Fig. 6 as they are quite insensitive to fluid pre-rotation [8].

In Fig. 6, the direct damping coefficients predicted using ANSYS Fluent and the results of Ha and Choe [25] agree with the experimental values both in terms of magnitude and trend. However, the OpenFOAM-predicted damping coefficients are nearly zero for all pressure ratios. The root-cause for this deficiency of the solver `steadyCompressibleSRFFoam` remains unclear. The governing equations and boundary conditions appear to be the same (or nearly so) in `steadyCompressibleSRFFoam` and ANSYS Fluent used in the present work. Moreover, algorithmic details related to the implementation of relative velocities and a rotating reference frame are similar between `steadyCompressibleSRFFoam` and `SRFSimpleFoam`, the latter of which accurately predicted dynamic coefficients for all the water seals considered previously. However, it is clear from Fig. 7b that striking differences exist in the dynamic pressures predicted by the compressible OpenFOAM and ANSYS Fluent solvers.

In Fig. 7b, the circumferential pressure distributions of the gas seal [57] at the seal mid-span are plotted for three different whirling amplitudes. Notably, the OpenFOAM predicted pressures in Fig. 7b fail to exhibit the asymmetry with respect to the circumferential direction necessary to give rise to the frequency-driven changes in tangential seal forces which would yield direct damping, see Eq. 2. In applying the whirling-rotor method, the pressure profiles along the seal circumference vary with frequency through the presence of additional Coriolis and centripetal accelerations, as well as the relative velocities imposed at the rotor and stator walls. Given that the predominant seal flow is in axial and circumferential directions, Coriolis and centripetal effects are restricted to acting in the radial direction and give rise to changes in the pressure profile amplitudes, visible in Fig. 7a, b. However, the circumferential phase shift in the pressure profile arising from the difference in the rotational speeds associated with rotor and stator surfaces, $\Omega - 2\omega$, is absent from Fig. 7b.

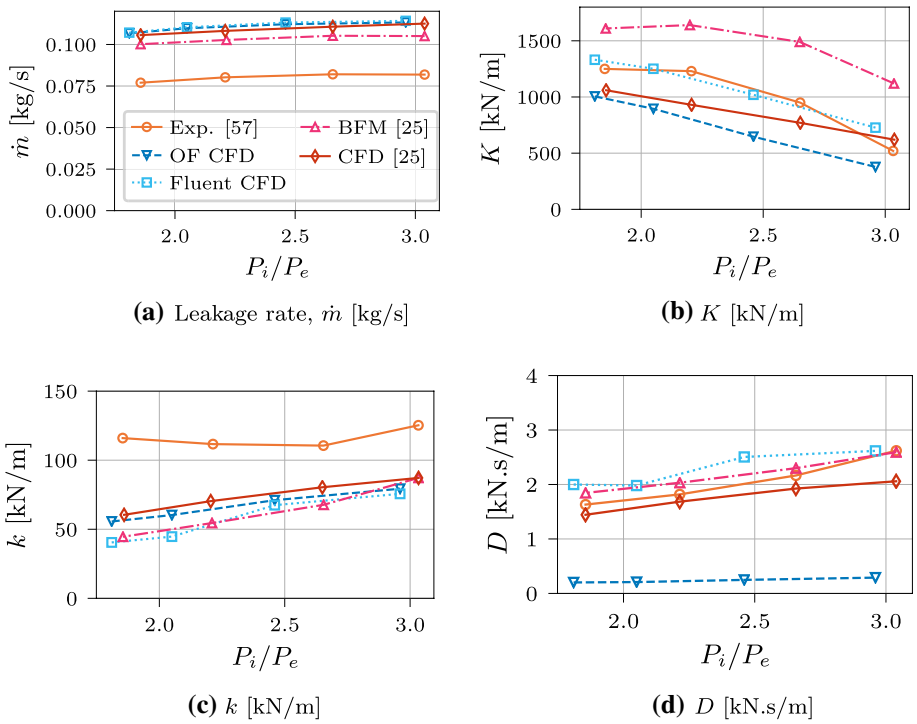

(a) Leakage rate, $\dot{m}$ [kg/s] **(b)** K [kN/m]

(c) k [kN/m] **(d)** D [kN.s/m]

Fig. 6 Variation in gas (air) seal [57] leakage and dynamic coefficients with pressure ratio at 5030 [rpm]. Present CFD results obtained with $SR = 0$ and $k - \omega$ SST turbulence model

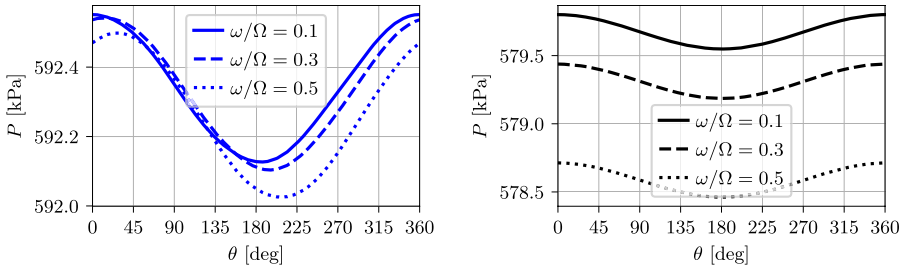

(a) ANSYS FLUENT v.19.0 **(b)** `steadyCompressibleSRFFoam`, OpenFOAM-extend-4.0

Fig. 7 Comparison of dynamic pressures at gas (air) seal [57] midspan. 5030 [rpm], $SR = 0$, $k-\omega$ SST turbulence model, $\Delta/C = 0.01$, and nominal mesh

The variation in the dynamic pressure predicted by ANSYS Fluent in Fig. 7a is as-expected with amplitude variation (normal to rotor) arising from centripetal and Coriolis forcing as well as phase variation (tangential to rotor) enabled through the difference between the rotor and stator rotational speeds, $\Omega - 2\omega$. Since ANSYS Fluent predicted the requisite asymmetry in the dynamic pressure profile, compressible flow simulations of the remaining seal geometries were exclusively performed with this software.

It appears that discrepancies in the compressible flow results obtained with OpenFOAM and ANSYS Fluent are due to differences in the implementation of the total pressure boundary conditions in the presence of a rotating reference frame. Specifically, the inlet boundary velocities used in computing the inlet Mach number do not appear to be computed in the same manner between the open-source and commercial codes. However, since the ANSYS Fluent source code is closed, the specific boundary condition implementation could not be examined.

6.2 Ransom and San Andrés [58] gas (air) seal

The gas seal [58] ($R = 63.45$ [mm], $C = 0.19$ [mm]) was modeled with pressure ratios P_i/P_e ranging from 1.25 to 3.0 and a rotor speed of 3600 [rpm].

The predicted leakage rates are summarized in Fig. 8. CFD-predictions agree with the experimental values and are slightly (but consistently) higher than the leakage rates predicted by the compressible BFMs [12, 58] at higher pressure ratios. The model-predicted leakage rates all fall within the uncertainty bounds of the repeated experimental measurements.

The direct stiffness coefficients in Fig. 8 predicted by the present CFD model agree well with the BFM results of [12] at lower pressure ratios, but the values begin to diverge from each other at larger pressure ratios. This is similarly true of the direct damping coefficients in Fig. 8.

Both the present CFD model and the BFM [12] predictions of stiffness and damping coefficients exhibit reasonable agreement with the experimental values except at pressure ratios of 1.75 and 2.0. At these pressure ratios, the experimental stiffness dips (even becomes slightly negative) and the damping spikes. It not wholly clear as to the cause of this "peculiar behavior" [58], but it does appear that the experimental natural frequencies were not as easily identified in the transfer functions for pressure ratios of 1.75 and 2.0 compared with the remaining pressure ratios and may have negatively impacted the dynamic coefficient estimates.

6.3 Elrod et al. [44] gas (air) seal 'C01'

The final gas seal considered was the 'C01' seal tested by Elrod et al. [44] ($R = 75.68$ [mm], $C = 0.7366$ [mm]). The pressure ratios varied from 1.5 to 2.6 with the exit pressure fixed at 1 [bar] and a rotor speed of 2000 [rpm]. The present CFD-predicted leakage rates in Fig. 9 closely agree with the experimental values and the CFD-based predictions of Nordmann et al. [59]. Reasonable agreement is also observed

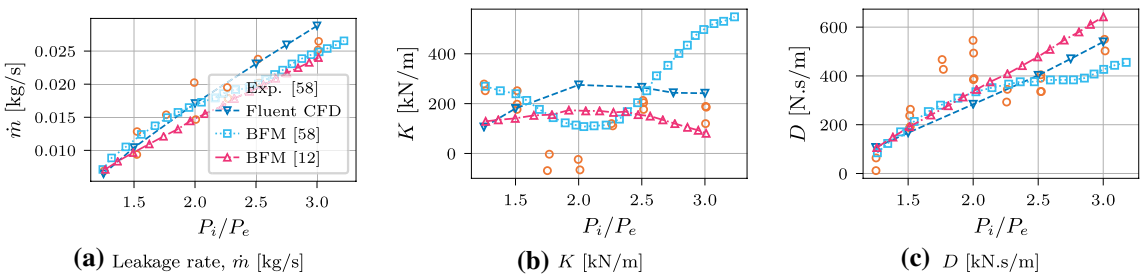

(a) Leakage rate, $\dot{m}$ [kg/s] **(b)** K [kN/m] **(c)** D [kN.s/m]

Fig. 8 Variation in gas (air) seal [58] leakage and dynamic coefficients with pressure ratio at 3600 [rpm]. Present CFD results obtained with $SR = 0$ and $k-\omega$ SST turbulence model

between the CFD-predicted and experimental direct stiffness and damping coefficients in Fig. 9b, c, respectively. While both the leakage rate and direct damping coefficient increase linearly with increasing pressure ratio, the direct stiffness of the seal remains nearly constant.

7 Conclusions

The whirling-rotor method was successfully applied using the OpenFOAM solver `SRFSimpleFoam` to accurately predict the axial pressure drops and dynamic coefficients of three smooth, annular, water pump seals. The OpenFOAM solver `steadyCompressibleSRFFoam` produced unsatisfactory results for the damping coefficients of gas seals. However, the whirling-rotor method implemented in ANSYS Fluent predicted leakage rates and dynamic coefficients for three smooth, annular, gas seals which wholly agreed with their experimental values, not accounting for the "peculiar behavior" in the experimental stiffness and damping coefficients of one gas seal [58]. The results obtained support the following conclusions regarding the numerical modeling approach:

1. For the large-R e annular, seal flows considered, accurate and consistent results could only be obtained with OpenFOAM for meshes with $y^+ \approx 1$ at the rotor and stator walls and at least 15 mesh cells distributed across the seal clearance. These requirements resulted in much larger overall mesh size compared with those of previous CFD investigations of annular seals.
2. Use of the $k-\omega$ family of turbulence models provided more accurate predictions of axial pressure drop and radial forces over the $k-\epsilon$ family of turbulence models.
3. Application of the $k-\epsilon$ family of turbulence models in OpenFOAM resulted in significant over-prediction of axial pressure drops and stiffness coefficients which correlated with elevated predictions of turbulent eddy viscosity across the seal clearance.
4. For the whirling-rotor method, applying a whirling amplitude $\Delta = 0.2C$ explicitly to the CFD mesh provided a reasonable balance between suppressing numerical error and satisfying the linear assumption of the dynamic seal force response.
5. The trends in CFD-predicted dynamic coefficients for varying inlet swirl mirrored those for bulk-flow models.
6. CFD predictions of damping coefficients and axial pressure drop for water seals were found to be less accurate for short seals, with the inflow and outflow regions of the seal geometry affecting behavior more than in long seals. This supports the application of CFD over BFM to model short seals as the inflow and outflow regions can be directly modeled.
7. For the water seals considered, the CFD-predicted dynamic coefficients and leakage rates closely agreed with the experimental values and incompressible bulk-flow predictions, except for the added mass coefficients of the longest seal [50] considered.
8. For the gas seals considered, the CFD-predicted leakage rates and dynamic coefficients were found to be at least as accurate as bulk-flow model predictions.
9. The tangential forces predicted using `steadyCompressibleSRFFoam` failed to exhibit the perturbation frequency dependence necessary to accurately predict damping coefficients of the gas seals. This deficiency was not observed in using the commercial CFD software ANSYS Fluent.

This precursory work has partially verified and validated the application OpenFOAM in predicting the rotordynamic performance for a selection of simple, annular seals subject to both incompressible and compressible flows. The results presented herein can be used to guide the setup and usage of CFD in the analysis of seal geometries with more complex flow features and for which bulk-flow models are insufficient.

Appendix

See Table 7.

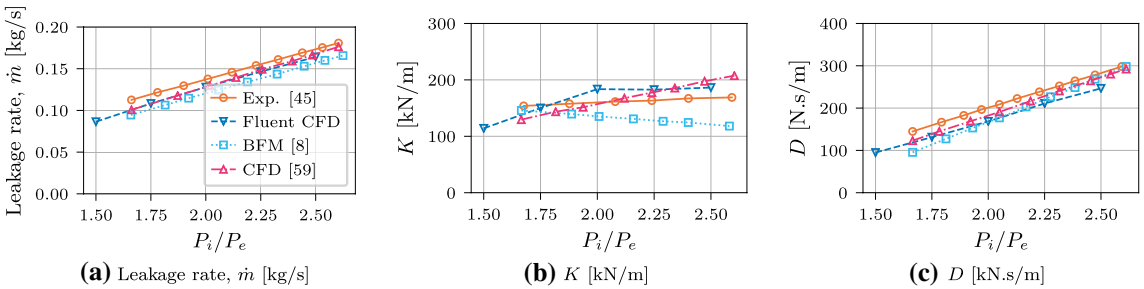

Fig. 9 Variation in gas (air) seal 'C1' [44] leakage and dynamic coefficients with pressure ratio at 2000 [rpm]. Present CFD results obtained with $SR = 0$ and $k-\omega$ SST turbulence model

Table 7 Mesh parameters tested for Kanki seal 1 [50]. r is the inflation layer growth ratio and y^+ values are rotor averages evaluated using OpenFOAM post-simulation

mesh	N_r	N_a	N_θ	r	y^+
a	10	25	78	1	30.8
b	10	96	303	58	1.58
c	10	190	550	115	0.837
d	10	250	800	147	0.659
e	15	37	115	1	22.3
f	15	110	345	44	1.56
g	15	190	550	87	0.872
h	15	240	550	112	0.702
i	15	280	620	112	0.702
j	20	50	157	1	15.8
k	20	99	314	30	1.57
l	20	190	550	61	0.887
m	20	240	550	80	0.711

Funding This project has received funding from the European Union's Horizon 2020 research and innovation programme under the Marie Skłodowska-Curie Grant Agreement No. 754462.

References

1. Hirs GG (190) Fundamentals of a bulk-flow theory for turbulent lubricant films. Ph.D. thesis, University of Technology Delft
2. Hirs GG (1973) A bulk-flow theory for turbulence in lubricant films. J Lubr Technol 95(2):137. https://doi.org/10.1115/1.3451752
3. Frêne J, Arghir M, Constantinescu V (2006) Combined thin-film and Navier-Stokes analysis in high Reynolds number lubrication. Tribol Int 39(8):734. https://doi.org/10.1016/j.triboint.2005.07.004
4. Black H (1969) Effects of hydraulic forces in annular pressure seals on the vibrations of centrifugal pump rotors. J Mech Eng Sci 11(2):206
5. Black H, Jenssen D (1970) Dynamic hybrid bearing characteristics of annular controlled leakage seals. Proc Inst Mech Eng 184:92
6. Childs DW (1983) Dynamic analysis of turbulent annular seals based on Hirs' lubrication equation. J Lubr Technol 105(3):429. https://doi.org/10.1115/1.3254633
7. Childs DW (1983) Finite-length solutions for rotordynamic coefficients of turbulent annular seals. J Lubr Technol 105(3):437. https://doi.org/10.1115/1.3254636
8. Nelson C (1985) Rotordynamic coefficients for compressible flow in tapered annular seals. J Tribol 107(3):318. https://doi.org/10.1115/1.3261062
9. Launder B, Leschziner M (1978) Flow in finite-width, thrust bearings including inertial effects: I-laminar flow. J Lubr Technol 100(3):330. https://doi.org/10.1115/1.3453181
10. Launder B, Leschziner M (1978) Flow in Finite-Width Thrust Bearings Including Inertial Effects: II-Turbulent Flow. J Lubr Technol 100(3):339. https://doi.org/10.1115/1.3453182
11. San Andrés LA (1991) Analysis of variable fluid properties, turbulent annular seals. J Tribol 113(4):694. https://doi.org/10.1115/1.2920681
12. Arghir M, Frêne J (2001) Numerical solution of lubrication's compressible bulk flow equations: applications to annular gas seals analysis. In: Turbo expo: power for land, sea, and air, vol 3. https://doi.org/10.1115/2001-GT-0117. V003T01A004
13. Przekwas AJ, Athavale MM (1992) Development of a CFD code for fluid dynamic forces in seals. In: Proceedings of the 1992 seals flow development workshop (CP-10124). NASA Lewis Research Center, Cleveland, pp 68–84
14. Nielsen KK, Jønck K, Underbakke H (2012) Hole-pattern and honeycomb seal rotordynamic forces: validation of CFD-based prediction techniques. J Eng Gas Turbines Power 134(12):122505. https://doi.org/10.1115/1.4007344
15. Dietzen F, Nordmann R (1987) Calculating rotordynamic coefficients of seals by finite-difference techniques. ASME J Tribol 109(3):388. https://doi.org/10.1115/1.3261453
16. Athavale M, Hendricks R (1996) A small perturbation CFD method for calculation of seal rotordynamic coefficients. Int J Rotating Mach 2(3):167. https://doi.org/10.1155/S1023621X96000048
17. Baskharone EA, Hensel SJ (1991) A finite-element perturbation approach to fluid/rotor interaction in turbomachinery elements. Part 1: Theory J Fluids Eng 113(3), 353. https://doi.org/10.1115/1.2909504
18. Baskharone EA, Hensel SJ (1991) A finite-element perturbation approach to fluid/rotor interaction in turbomachinery elements. Part 2: Appl J Fluids Eng 113(3):362. https://doi.org/10.1115/1.2909505
19. Arghir M, Frêne J (1997) Forces and moments due to misalignment vibrations in annular liquid seals using the averaged Navier-Stokes equations. J Tribol 119(2):279. https://doi.org/10.1115/1.2833194
20. Patankar SV, Spalding DB (1972) Numerical predictions of three-dimensional flows. Tech. Rep. MED Rep. EF/TN/A/46, Imperial College, London (1972)
21. Patankar SV (1980) Numerical heat transfer and fluid flow. CRC Press, Boca Raton
22. Tam LT, Przekwas AJ, Muszynska A, Hendricks RC, Braun MJ, Mullen RL (1988) Numerical and analytical study of fluid dynamic forces in seals and bearings. J Vib Acoustics Stress Reliab Design 110(3):315. https://doi.org/10.1115/1.3269519
23. Athavale M, Hendricks RC, Steinetz BM (1995) Numerical simulation of flow in a whirling annular seal and comparison with experiments. Tech. Rep. TM 106961, NASA (1995)
24. Moore JJ, Palazzolo AB (2001) Rotordynamic force prediction of whirling centrifugal impeller shroud passages using computational fluid dynamic techniques. J Eng Gas Turbines Power (Trans ASME) 123(4):910. https://doi.org/10.1115/1.2900958
25. Ha TW, Choe BS (2014) Numerical prediction of rotordynamic coefficients for an annular-type plain-gas seal using 3D CFD analysis. J Mech Sci Technol 28(2):505. https://doi.org/10.1007/s12206-011-0830-3
26. Moore JJ (2003) Three-dimensional CFD rotordynamic analysis of gas labyrinth seals. J Vib Acoust 125(4):427. https://doi.org/10.1115/1.1615248
27. Tsukuda T, Hirano T, Watson C, Morgan NR, Weaver BK, Wood HG (2018) A numerical investigation of the effect of inlet preswirl ratio on rotordynamic characteristics of labyrinth seal. J Eng Gas Turbines Power 140(8):082506. https://doi.org/10.1115/GT2017-64745
28. Ha TW, Choe BS (2012) Numerical simulation of rotordynamic coefficients for eccentric annular-type-plain-pump seal using CFD analysis. J Mech Sci Technol 26(4):1043. https://doi.org/10.1007/s12206-012-0217-x

29. Untaroiu A, Untaroiu CD, Wood HG, Allaire PE (2013) Numerical modeling of fluid-induced rotordynamic forces in seals with large aspect ratios. J Eng Gas Turbines Power 135(1):012501. https://doi.org/10.1115/1.4007341
30. Kim SH, Ha TW (2016) Prediction of leakage and rotordynamic coefficients for the circumferential-groove-pump seal using CFD analysis. J Mech Sci Technol 30(5):2037. https://doi.org/10.1007/s12206-016-0410-4
31. Chochua G, Soulas TA (2007) Numerical modeling of rotordynamic coefficients for deliberately roughened stator gas annular seals. J Tribol 129(2):424. https://doi.org/10.1115/1.2647531
32. Voigt AJ, Iudiciani P, Nielsen KK, Santos IF (2016) CFD applied for the identification of stiffness and damping properties for smooth annular turbomachinery seals in multiphase flow. In: ASME Turbo Expo 2016: turbomachinery technical conference and exposition (American Society of Mechanical Engineers, 2016), pp V07BT31A034–V07BT31A034. https://doi.org/10.1115/GT2016-57905
33. Weller HG, Tabor G, Jasak H, Fureby C (1998) A tensorial approach to computational continuum mechanics using object-oriented techniques. Comput Phys 12(6):620. https://doi.org/10.1063/1.168744
34. OpenFOAM (2019) OpenFOAM ver. 5.x. https://doi.org/10.1115/1.29009580
35. OpenFOAM (2019) OpenFOAM-extend ver. 4.0. https://doi.org/10.1115/1.29009581
36. ANSYS®, Fluent Release Version 19.1, User Guide (2019)
37. ANSYS®, Fluent Release Version 19.1, Theory Guide (2019)
38. Wagner C, Sinzig S, Thümmel T, Rixen D (2018) Calculating rotordynamic coefficients of liquid annular seals by CFD for vibration analysis and validation at the Test Rig. In: International conference on rotor dynamics. Springer, New York, pp 397–410. https://doi.org/10.1007/978-3-319-99262-4_29
39. Wilcox DC et al (1998) Turbulence modeling for CFD, vol 2. DCW industries La Canada, CA
40. Swamee P, Jain A (1976) Explicit equations for pipe-flow problems. J Hydraulics Div 102(5):657
41. Spalding D (1961) A single formula for the "law of the wall". J Appl Mech 28(3):455
42. Jasak H (1996) Error analysis and estimation for the finite volume method with applications to fluid flows. Ph.D. thesis, Imperial College, University of London (1996)
43. Ferziger JH, Perić M (2002) Computational methods for fluid dynamics, 3rd edn. Springer, New York
44. Elrod D, Nicks C, Childs D, Nelson C (1985) A comparison of experimental and theoretical results for rotordynamic coefficients of four annular gas seals. NASA Progress Report NASA-CR-176086, Texas A&M University, College Station
45. Childs D (1993) Turbomachinery rotordynamics: phenomena, modeling, and analysis. Wiley, Hoboken
46. Constantinescu VN, Galetuse S (1974) On the possibilities of improving the accuracy of the evaluation of inertia forces in laminar and turbulent films. J Tribol 96(1):69. https://doi.org/10.1115/1.3451912
47. White FM (1998) Fluid mechanics, 4th edn. McGraw-Hill, London
48. Nelson CC, Nguyen DT (1987) Comparison of Hirs' equation with Moody's equation for determining rotordynamic coefficients of annular pressure seals. J Tribol 109(1):144. https://doi.org/10.1115/1.3261306
49. Childs D, Nelson C, Nicks C, Scharrer J, Elrod D, Hale K (1986) Theory versus experiment for the rotordynamic coefficients of annular gas seals: Part 1-Test facility and apparatus. J Tribol 108(3):426. https://doi.org/10.1115/1.3261226
50. Kanki H, Kawakami T (1984) Experimental study on the dynamic characteristics of pump annular seals, IMechE, paper, pp 159–166
51. Celik IB, Ghia U, Roache PJ, Freitas CJ, Coleman H, Raad PE (2008) Procedure for estimation and reporting of uncertainty due to discretization in CFD applications. J Fluids Eng 130(7):78001. https://doi.org/10.1115/1.2960953
52. Menter FR (1994) Two-equation eddy-viscosity turbulence models for engineering applications. AIAA J 32(8):1598. https://doi.org/10.2514/3.12149
53. Massmann H (1986) Ermittlung der dynamischen Parameter axial turbulent durchströmter Ringspalte bei inkompressiblen Medien. Ph.D. thesis, Universität Kaierslautern (1986)
54. Simon F, Frêne J (1989) Static and dynamic characteristics of turbulent annular eccentric seals: effect of convergent-tapered geometry and variable fluid properties. J Tribol 111(2):378. https://doi.org/10.1115/1.3261927
55. Simon F, Frêne J (1992) Analysis for incompressible flow in annular pressure seals. J Tribol 114(3):431. https://doi.org/10.1115/1.2920902
56. Simon J, Frêne J (1990) Rotordynamic coefficients for turbulent annular misaligned seals. In: 3rd International symposium on transport phenomena and dynamics of rotating machinery, vol 2. Honolulu, Hawaii
57. Dunn MS (1990) A comparison of experimental results and theoretical predictions for the rotordynamic coefficients of stepped annular gas seals. Master's thesis, Texas A&M (1990)
58. Ransom DL, San Andrés L (1999) Identification of force coefficients from a gas annular seal-effect of transition flow regime to turbulence. Tribol Trans 42(3):487. https://doi.org/10.1080/10402009908982245
59. Nordmann R, Dietzen F, Weiser H (1989) Calculation of rotordynamic coefficients and leakage for annular gas seals by means of finite difference techniques. J Tribol 111(3):545. https://doi.org/10.1115/1.3261964